# Zinc induced folding is essential for TIM15 activity as an mtHsp70 chaperone

**ARTICLE** *in* BIOCHIMICA ET BIOPHYSICA ACTA · JANUARY 2013

Impact Factor: 4.66 · DOI: 10.1016/j.bbagen.2012.10.002 · Source: PubMed



**5 AUTHORS**, INCLUDING:

Hugo Fraga
Institut de Biologie Structurale, Grenoble
**25** PUBLICATIONS **497** CITATIONS
SEE PROFILE

Elena Papaleo
Danish Cancer Society
**58** PUBLICATIONS **605** CITATIONS
SEE PROFILE

Adrian Velazquez-Campoy
University of Zaragoza
**119** PUBLICATIONS **2,211** CITATIONS
SEE PROFILE

Salvador Ventura
Autonomous University of Barcelona
**161** PUBLICATIONS **3,496** CITATIONS
SEE PROFILE

Biochimica et Biophysica Acta 1830 (2013) 2139–2149

Contents lists available at SciVerse ScienceDirect

Biochimica et Biophysica Acta

journal homepage: www.elsevier.com/locate/bbagen

# Zinc induced folding is essential for TIM15 activity as an mtHsp70 chaperone

Hugo Fraga [a,b,*], Elena Papaleo [b,c], Sonia Vega [d], Adrián Velazquez-Campoy [d,e], Salvador Ventura [a,b,**]

[a] Departament de Bioquímica i Biologia Molecular, Facultat de Biociències, Universitat Autònoma de Barcelona, E-08193 Bellaterra Spain
[b] Institut de Biotecnologia i de Biomedicina, Universitat Autònoma de Barcelona, E-08193 Bellaterra Spain
[c] Department of Biotechnology and Biosciences, University of Milano-Bicocca, Piazza della Scienza 2, 20126 Milan, Italy
[d] Institute of Biocomputation and Physics of Complex Systems, Unidad Asociada IQFR-CSIC-BIFI, Universidad de Zaragoza, Zaragoza, Spain
[e] Fundación ARAID, Diputación General de Aragón, Spain

ARTICLE INFO

*Article history:*
Received 18 June 2012
Received in revised form 21 September 2012
Accepted 3 October 2012
Available online 11 October 2012

*Keywords:*
TIM15
Mitochondrion
Protein folding
Zinc finger
Protein translocation

ABSTRACT

*Background:* TIM15/Zim17 in yeast and its mammalian ortholog Hep are $Zn^{2+}$ finger (Cys4) proteins that assist mtHsp70 in protein import into the mitochondrial matrix.
*Methods:* Here we characterized the $Zn^{2+}$ induced TIM15 folding integrating biophysical and computational approaches.
*Results:* TIM15 folding occurs from an essentially unstructured conformation to a $Zn^{2+}$-coordinated protein in a fast and markedly temperature-dependent process. Moreover, we demonstrate unambiguously that $Zn^{2+}$ induced TIM15 folding is essential for its role as mtHsp70 chaperone since in the unstructured apo state TIM15 does not bind to mtHsp70 and is unable to prevent its aggregation. Molecular dynamics simulations help to understand the crucial role of $Zn^{2+}$ in promoting a stable and functional 3D architecture in TIM15. It is shown that the metal ion, through its coordinating cysteine residues, can mediate relevant long-range effects with the interaction interface for mtHsp70 coupling thus folding and function.
*Conclusions:* $Zn^{2+}$ induced TIM15 folding is essential for its function and likely occurs in mitochondrial matrix where high concentrations of $Zn^{2+}$ were reported.
*General significance:* The combination of experimental and computational approaches presented here provide an integrated structural, kinetic and thermodynamic view of the folding of a mitochondrial zinc finger protein, which might be relevant to understand the organelle import of proteins sharing this fold.


## 1. Introduction

Mitochondria are fundamental for many cellular processes that include energy metabolism, apoptosis and diverse metabolic pathways. About 98% of mitochondrial proteins are encoded in the nucleus, translated in the cytosol and imported to the organelle to acquire their functional states [1,2]. In order to achieve mitochondrial import most of them, if not all, have to be in a translocation competent conformation, that includes being unfolded, stabilized by cytosolic cofactors (Hsp70 and Hsp90) [2] and endowed with organelle targeting signals [3,4].

The mitochondrial Hsp70 (mtHsp70; also called Ssc1 in yeast and mortalin/HSA9 in mammals) binds proteins in transit and is one of the components of the mitochondrial protein import machinery. Precursor proteins encounter mtHsp70 immediately upon entry of the terminus of the unfolded polypeptide in the matrix where mtHsp70 provides the driving force for translocation of polypeptides through the TIM23 complex [3].

TIM15 [5], also named Zim17 from its Zinc finger motif and 17 kDa molecular mass [6] and Hep1 (DNLZ/Hep in humans) for mHsp70 escort protein [7,8] are peripheral inner membrane proteins facing the matrix that assist mtHsp70 in protein import into the mitochondria matrix [5,6,8,9].

It has been proposed that TIM15/Hep primary function is as mtHsp70-specific chaperone and in fact its role was demonstrated in vivo [7–9]. Deletion of TIM15 in yeast results in mHsp70 aggregation, an effect that cannot be counteracted by mtHsp70 overexpression [8,9]. Additionally, using heterologous expression in *Escherichia coli* it was observed that, while the expression of mtHsp70 results in insoluble protein, its coexpression with TIM15 or Hep (despite the 25% homology with the human homolog, yeast TIM15 is able to promote the solubility of human mtHsp70), results in significant amounts of soluble mtHsp70 [7–10]. Moreover, using purified proteins and crosslinking, Sichting et

*Abbreviations:* AMS, (4-acetamido-49-maleimidylstibene-2,29-disulfonic acid); ANS, 8-anilino-1-naphthalenesulfonic acid; DCCM, dynamical cross-correlation matrix; DSC, differential scanning calorimetry; DTT, dithiothreitol; EDTA, ethylene diamine tetraacetic acid; ITC, isothermal titration calorimetry; MD, molecular dynamics; PSN, protein structure network; TCEP, tris(2-carboxyethyl)phosphine; ThT, thioflavin T

* Correspondence to: H. Fraga, Institut de Biotecnologia i de Biomedicina, Universitat Autònoma de Barcelona, E-08193 Bellaterra Spain. Tel.: +34 93 5812154; fax: +34 93 5811264.
** Correspondence to: S. Ventura, Institut de Biotecnologia i de Biomedicina, Universitat Autònoma de Barcelona, E-08193 Bellaterra Spain. Tel.: +34 93 5868956; fax: +34 93 5811264.
*E-mail addresses:* hugofraga@gmail.com (H. Fraga), salvador.ventura@uab.es (S. Ventura).

0304-4165/$ – see front matter © 2012 Elsevier B.V. All rights reserved.
http://dx.doi.org/10.1016/j.bbagen.2012.10.002

al. [8] demonstrated that TIM15 binds to mtHsp70 in the nucleotide free state, preventing the formation of mtHsp70 oligomeric species; similar results have been reported using gel filtration by Zhai and coworkers [7,8]. Recently, it was shown that Hep stably interacts with the isolated mtHsp70 ATPase domain and the analysis of the solubility of different mtHsp70 fragments has shown that the N-terminal region containing the ATPase domain together with a small interdomain linker is prone to aggregation while the C-terminal substrate binding (SBD) domain is by itself soluble [10]. The interaction between Hep and the mtHsp70 ATPase domain is certainly linked to the Hep activating effect on the ATPase activity but the molecular mechanism responsible for that effect remains elusive. Contrary to GrpE, Hep is not a nucleotide exchange factor [11] and although it interacts with the SBD it does not compete with mtHsp70 canonical substrates [11]. Curiously, despite TIM15 and Hep proteins having been shown to be interchangeable, for example Hep is able to complement ΔTIM15 yeast, TIM15 is unable to activate yeast mtHsp70 ATPase activity in a clear mechanistic difference between the orthologous proteins [8,12].

Taking in consideration its links to mtHsp70, it is not surprising that TIM15/Hep deletion results in phenotypes that mimic mtHsp70 deficiency, namely anomalies in the import of mitochondrial preproteins and in the biogenesis of FeS proteins [6,8,13]. More recently an association between TIM15 and genome instability was demonstrated [14]. Another study also suggests that TIM15 chaperone activity may not be limited to mtHsp70 as, at least in vitro, TIM15 was able to assist in the folding of rhodanese [11]. Accordingly, TIM15 has been shown to bind unfolded mitochondrial proteins [6].

Although a considerable amount of information is already available on TIM15, several key points remain to be clarified. TIM15 contains a 4 cysteine $Zn^{2+}$ finger motif and its metal loaded structure has been determined [9]. However, considering that TIM15 is nuclear encoded, it is probable that it is its apo state that is translocated trough the outer and inner mitochondrial membranes and that $Zn^{2+}$ coordination will occur in the mitochondria matrix. Moreover, since TIM15 and Hep contain typical N-terminal targeting sequences, it is likely that its import is mediated by the Tim23 pathway and itself chaperoned by mtHsp70 representing a curious case of co-chaperoning, where one chaperone assists the other sequentially [8]. Here we described a biophysical and computational characterization of $Zn^{2+}$ induced TIM15 folding. As described for other $Zn^{2+}$ finger proteins, metal coordination results in the highly exothermic formation of a hydrophobic core. We show that $Zn^{2+}$ coordination is fundamental for TIM15 chaperone activity, as only the folded protein has an affinity for the mtHsp70. TIM15 folding is a fast process that depends exclusively on the formation of the $Zn^{2+}$ finger motif.

## 2. Materials and methods

### 2.1. Protein expression and purification

TIM15c, GST-TIM15 fusion and Ssc1were expressed in *E. coli* and purified as described in [9]. Pull down assays were done as described in [9] with the exception that EDTA was included to obtain apo-TIM15-GST.

### 2.2. Thioflavin T aggregation assay

Ssc1 (10 μM) in phosphate buffer 50 mM pH 7.0 and thioflavin T (25 μM) were mixed with TIM15c (10 μM) with or without EDTA (200 μM) and fluorescence (excitation 450 nm; emission 480 nm) was measured at 0.55 min intervals during at least 8000 min. A sample with TIM15c (10 μM) plus EDTA (200 μM) was run as a control. For the analysis of Scs1 aggregation rates as a function of TIM15c concentration the same protocol was followed except that different concentrations of TIM15c were used. The aggregation rates were plotted and fitted to a single binding site equation using Prism (GraphPad).

### 2.3. AMS shift assay

TIM15c (0.2 mg/ml) was incubated overnight in the absence or in the presence of the reductive agent TCEP (10 mM) and to this mixture (10 μl) was added an equal volume of AMS (20 mM) in 2× SDS buffer, incubated in the dark for an hour and loaded in a 16% SDS-PAGE Tricine gel.

### 2.4. CD spectroscopy

Far UV CD spectra were acquired on a Jasco-710 spectropolarimeter continuously purged with nitrogen and thermostated at 298 K. A TIM15c (7 μM) protein solution was prepared in 5 mM sodium acetate pH 4.5, containing 1 mM TCEP and 10 mM NaCl. To evaluate the effect of $Zn^{2+}$ over the protein, assays were carried out in the absence (EDTA 1 mM) and in the presence of $ZnCl_2$ (50 μM). Scans were collected using a 0.2 mm path length cuvette, between 200 and 260 nm at 1 nm intervals.

### 2.5. Proteinase K digestion

Proteinase K to a final concentration of 10 μg/ml was added to a mixture containing TIM15c (0.1 μM) in sodium acetate pH 4.5 (20 mM), NaCl (50 mM), DTT (1 mM) and $Zn^{2+}$ (50 μM) or EDTA (1 mM) at room temperature. Aliquots of the reaction mixtures were removed at the indicated times and mixed with SDS sample buffer with Pefabloc (Sigma-Aldrich) 1 mM. Samples were loaded in a 16% SDS-PAGE Tricine gel.

### 2.6. Fluorescence spectroscopy

Intrinsic tyrosine fluorescence was measured using TIM15c (20 μM) in the absence (1 mM EDTA) or presence of $Zn^{2+}$ (50 μM). The spectra were measured in the 280–350 nm interval using a 274 nm excitation wavelength (10 nm excitation and emission slits, 0.1 s averaging time). ANS fluorescence was measured in the same conditions as described for folding kinetics, namely using a 50 μM of TIM15c and 100 μM ANS solution in the presence of 200 μM EDTA to which an equal volume of buffer or $Zn^{2+}$ solution (500 μM) was added. Fluorescence emission spectra were measured in the 400–550 nm interval using 380 nm as excitation wavelength for ANS (5 nm excitation and emission slits, 0.1 s averaging time).

### 2.7. Folding kinetics

TIM15c folding kinetics was measured using ANS as a probe in a Bio-Logic SFM-3 stopped flow with a 480 nm emission filter. Briefly, a solution containing TIM15c (50 μM), EDTA (200 μM) and ANS (100 μM) was mixed (1:1 ratio) with other containing $Zn^{2+}$ (500 μM) or buffer (negative control). The data was fitted to a single exponential equation with GraphPad Prism in order to get TIM15 folding rate.

### 2.8. Isothermal titration calorimetry (ITC)

$Zn^{2+}$ binding to TIM15 was determined with a high-sensitivity isothermal titration VP-ITC microcalorimeter (MicroCal, GE Healthcare). All solutions were properly degassed and carefully loaded into the cells to avoid bubble formation during stirring. Experiments were performed in 20 mM sodium acetate, pH 4.5, 50 mM sodium chloride, 1 mM DTT.

Since purified TIM15c is bound to $Zn^{2+}$ [9], $Zn^{2+}$-free TIM15c was obtained by adding EDTA, instead of performing a dialysis step. Thus, instead of removing cations using chelating resins and dialysis steps, EDTA was added in a slight excess to remove $Zn^{2+}$ from TIM15c and the bulk solution in the calorimetric cell. The binding affinity and enthalpy change for $Zn^{2+}$ binding to EDTA were independently

determined ($K_a = 4.9 \cdot 10^8\ M^{-1}$, $\Delta H = 3.7$ kcal/mol) under the same conditions, and were used in the protein binding data analysis.

A typical experiment was carried out titrating TIM15c (20 μM) plus EDTA (40 μM) in the calorimetric cell with $Zn^{2+}$ (350 μM) in the syringe. A sequence of 10 μl injections was programmed. In general, biphasic titrations are expected, in which injected $Zn^{2+}$ binds first to excess EDTA, and, then, as EDTA gets saturated, starts binding to TIM15c.

The heat associated with each ligand injection was obtained from the integral of the calorimetric signal. The heat due to the binding reaction was obtained as the difference between the reaction heat and the corresponding heat of dilution, the latter estimated as a constant heat throughout the experiment, and included as an adjustable parameter in the analysis. Data were analyzed using software developed in our laboratory implemented in Origin 7 (Origin Lab).

In general, the binding of cations to EDTA is strongly pH-dependent, and the same can be expected for the $Zn^{2+}$ binding to TIM15c. This dependency is caused by protonation/deprotonation events coupled to cation binding. Consequently, in general the thermodynamic binding parameters (association constant and binding enthalpy) determined for $Zn^{2+}$ binding will contain a contribution from the buffer ionization. The association constant will not contain a contribution from the buffer ionization as long as the experimental pH is close to the $pK_a$ of the buffer employed (pH = 4.5, $pK_a$(acetate) = 4.75). On the other hand, the contribution of the buffer ionization to the observed binding enthalpy depends on the number of protons exchanged between the protein and ligand complex and the bulk solution, and the buffer ionization enthalpy ($n_H \Delta H_{ion,buffer}$). Because the ionization enthalpy of acetate buffer is negligible ($\Delta H_{ion,acetate} = -0.1$ kcal/mol, [15]), the observed binding enthalpy will not be affected by the proton exchange process, no matter how many protons are exchanged. Therefore, performing the titration experiments at pH 4.5 in acetate buffer we will determine directly the buffer-independent binding parameters for TIM15/$Zn^{2+}$ interaction.

The data analysis for the calorimetric titration experiments has been described previously [16–18]. According to the solution structure (PDB code 2E2Z), TIM15c contains a single $Zn^{2+}$ binding site. Therefore, in titrations of TIM15 with $Zn^{2+}$ in the presence of EDTA two coupled binding equilibria must be considered:

$$\begin{aligned} M + L &\leftrightarrow ML \\ Q + L &\leftrightarrow QL \end{aligned} \quad (1)$$

where M refers to the protein (apoTIM15c), Q to the chelating agent (EDTA), and L to $Zn^{2+}$. The ternary equilibrium represented in Eq. (1) allows one to calculate the concentration of the complexes, [ML] and [QL], by solving the mass-conservation equation system:

$$\begin{aligned} [M]_T &= [M] + [ML] = [M] + K_a[M][L] \\ [Q]_T &= [Q] + [QL] = [Q] + K_Q[Q][L] \\ [L]_T &= [L] + [ML] + [QL] = [L] + K_a[M][L] + K_Q[Q][L] \end{aligned} \quad (2)$$

where $K_a$ and $K_Q$ are the association constants for $Zn^{2+}$ binding to TIM15c and EDTA, respectively. Then, the heat effect, $q_i$, associated with each injection i is given by:

$$q_i = V\left(\Delta H_M\left([ML] - [ML]_1\left(1 - \frac{v}{V}\right)\right) + \Delta H_Q\left([MQ] - [MQ]_{-1}\left(1 - \frac{v}{V}\right)\right)\right) \quad (3)$$

where $\Delta H_M$ and $\Delta H_Q$ are the enthalpies for $Zn^{2+}$ binding to TIM15c and EDTA, respectively, and v and V are the injection and calorimetric cell volumes, respectively. Non-linear regression analysis was performed with software developed in our laboratory and implemented in Origin 7.0 (OriginLab).

Experiments were performed at different temperatures (15, 20, 25 and 30 °C) for estimating the heat capacity change upon binding. The main contribution to this parameter is the change in solvent accessible surface area upon binding. Therefore, it may provide information about conformational changes in TIM15 coupled to $Zn^{2+}$ binding.

### 2.9. Differential scanning calorimetry (DSC)

The molar heat capacity of TIM15 was measured as a function of temperature with a high-sensitivity differential scanning VP-DSC microcalorimeter (MicroCal, GE Healthcare). Protein samples and reference solutions were properly degassed and carefully loaded into the cells to avoid bubble formation. The baseline of the instrument was routinely recorded before the experiments. Experiments were performed in 20 mM sodium acetate, pH 4.5, 50 mM sodium chloride, 1 mM DTT, at a scanning rate of 1 °C/min. Experiments were carried out with 40 μM of TIM15c in either the absence or the presence of $Zn^{2+}$ (100 μM). $Zn^{2+}$-free protein was obtained by adding a large excess of EDTA (>200 μM). Data were analyzed using software developed in our laboratory implemented in Origin 7 (OriginLab).

### 2.10. Molecular dynamics (MD) simulations

MD simulations were performed using Gromacs 4.5.3 software (www.gromacs.org) implemented on a parallel architecture, using the Amber99sb-ILDN* and, the Charmm27 force field [19]. The NMR structure of native holo-TIM15c (PDB entry 2E2Z [9]) was used as a starting point for one 100 ns MD simulations for each of the force field to assess the reproducibility of the results. There are no overall differences in the scenario described by the MD simulations carried out with the two different force fields, therefore results for Charmm27 calculations are discussed in details. Initial structure for the apo-form was obtained according to the following procedure: the $Zn^{2+}$ ion was removed from the PDB file and the resulting apo-TIM15 structure was optimized by molecular mechanics (1000 steepest descent cycles followed by 10,000 conjugate gradient steps). Both apo- and holo-TIM15c were then submitted to solvent equilibration, thermalization and pressurization steps (each of 100 ps). Holo- and apo-forms were soaked in a dodecahedral box of TIP3p water molecules and simulations were carried out using periodic boundary conditions. All the protein atoms were at a distance equal or greater than 0.7 nm from the box edges. The ionization state of the residues was set to be consistent with neutral pH and the tautomeric form of histidines was derived using Gromacs tools and confirmed by visual inspection and PROPKA predictions [20]. Productive MD simulations of 100 ns have been carried out in the isothermal–isobaric (NPT) ensemble at 300 K, using the Berendsen thermostat with a coupling constant of 0.1 ps. Pressure was kept constant (1 bar) by modifying the box dimensions and the time-constant for pressure coupling was set to 1 ps. The LINCS algorithm [21] was used to constrain heavy-atom bond lengths, allowing the use of 2 fs time step. Electrostatic interactions were calculated using the particle–mesh Ewald (PME) summation scheme [22]. Van der Waals and Coulomb interactions were truncated at 1.0 nm. The nonbonded pair list was updated every 10 steps and conformations stored every 4 ps.

To assess the conformational stability of the protein during the MD simulation, time-dependent root mean square deviation (RMSD) of the main chain atoms with respect to the initial structure was monitored. Both the holo- and apo-TIM15c simulations acquired a plateau in the first 5–10 ns of simulations with both the force fields. Therefore, the first 10 ns were discarded from further analyses in order to avoid artifacts. The distance between the $Zn^{2+}$ ion and the coordinating cysteine (C75, C78, C100 and C103 the numbering of TIM15) was monitored in the holo-TIM15 simulations to assess the stability of the $Zn^{2+}$ ion in the metal binding site.

### 2.11. Dynamical cross-correlation matrices (DCCM)

Correlation plots were obtained by computing Cα dynamical cross-correlation matrix (DCCM) $C(i,j)$ [23], using non over-lapping

averaging windows of 1 ns, and also compared, for validation, to correlations on averaging windows of 5 and 10 ns. $C(i,j)$ has been calculated according to,

$$C(i,j) = \frac{c(i,j)}{c(i,i)^{1/2}c(j,j)^{1/2}} \quad (4)$$

where $c(i,j)$ is the covariance matrix element of protein fluctuation between residues $i$ and $j$.

Only the most significant ($|C(i,j)|>0.35$) long-range ($|i-j|>8$) positive and negative correlations were considered. In fact, the cutoff of sequence distance was selected in order to exclude from the analysis correlations relative to regions contiguous in the primary sequence. Moreover, since we discuss an average $C(i,j)$ matrix, the cutoff of 0.35 (in absolute value) for significant correlation was selected to exclude from the analysis pairs of residues which are poorly communicating each other and likely to be characterized by uncoupled motions. To carefully verify that the analysis of an average $C(i,j)$ matrix did not cause a loss of relevant information, the consistency between the average $C(i,j)$ matrix with the individual matrices used in the averaging was evaluated. Correlations were then plotted on the 3D structures by connecting atoms $i$ and $j$ with lines, with thickness proportional to $C(i,j)$.

### 2.12. Protein structure networks (PSN) and shortest correlated path of communication

The protein structure network approach [24] was integrated to data from the DCCM analysis of the holo- and apo-TIM15c MD ensemble, to identify the most relevant communication pathways between the residues coordinating the $Zn^{2+}$ ion (C75, C78, C100 and C103) and each residue of the protein structure, following an approach previously applied to other enzymes [25–27]. The PSN method employs the graph formalism to define a network of interacting residues in a given protein or protein complex from the number of non-covalent interacting atoms, using a calculated $I_{ij}$ interaction strength value as the edge weight, where $i$ and $j$ are residue identifiers. This value is calculated on the basis of the number of distinct atom pairs between residues $i$ and $j$ within a distance cut-off of 4.5 Å ($n_{ij}$):

$$I_{ij} = \frac{n_{ij}}{\sqrt{N_i N_j}} * 100 \quad (5)$$

where $N_i$ and $N_j$ are normalization values for residues $i$ and $j$ obtained from a statistically significant protein dataset. Nodes are connected to edges if $I_{ij}>I_{min}$. $I_{min}$ was set equal to $I_{crit}$, where $I_{crit}$ is the value of $I_{min}$ at which the size of the largest clusters in the graph significantly changes [25,27]. To obtain a single PSN for each MD trajectory, a single PSN network was calculated for each frame and only edges present in at least half of the simulation frames were considered. For each pair of selected residues, the Floyd–Warshal algorithm was used to determine the shortest path between selected pairs of nodes in the PSN graph. The distance between connected residues was considered to be 1, and the shortest path was identified as the path in which the two residues were non-covalently connected by the smallest number of intermediate nodes. Only the shortest paths in which at least one identified node featured a significant correlation value (>0.35) with one of the residues of the selected pairs were retained. All the PSN and PSN-DCCM calculations were performed using the WORDOM MD trajectories analysis suite [28].

### 2.13. Principal component analysis (PCA)

PCA reveals high-amplitude concerted motion in MD trajectories, through the eigenvectors of the mass-weighted covariance matrix (C) of the Cα atomic positional fluctuations [29]. In our trajectories, the first three eigenvectors describe generally more than 60% of the total motion, and the first principal component accounts itself for about the 40% of the total variance in both the apo and holo-TIM15 simulations.

### 2.14. Intramolecular interactions in the MD ensemble

Salt bridges and their networks, along with networks of aromatic, cation-PI and hydrophobic interactions, were analyzed employing a persistence cut-off of 20% and a distance cutoff of 0.5 nm. Aromatic interactions have also been checked at a higher cutoff of 0.6 nm. Since the output is based on a distance cutoff, the electrostatic interactions were carefully pruned considering only the ones in which the orientation of the angle between the interacting residues is appropriate.

The persistence cutoff of 20% was selected as the persistence value that best divided the interaction dataset in well-separated groups, defines as signal and noise, according to a protocol previously applied [30]. To identify clusters of spatial proximity of salt bridges, the residues involved in ion pairs were represented as nodes of an unrooted unoriented graph, in which two nodes were connected by arcs if a salt bridge was identified between them or if they were at less than five residues of distance in the sequence. An exhaustive search procedure was carried out on the graph to isolate the spatial proximity clusters of salt bridges and their networks.

## 3. Results

So far, the effect of $Zn^{2+}$ on TIM15 function has been mostly studied with the introduction of mutations or domain truncations that are expected to abolish metal coordination and the analysis of mtHsp70 solubility upon co-expression in *E. coli* [9,11,12,31]. However, the interpretation of those results is often complex because the effect of these modifications on TIM15 folding must also be considered. For example, it has been reported that the mutation of the $Zn^{2+}$ chelating cysteines to serine abolish Hep solubility [7]. Additionally, it has been observed that the folding in *E. coli*, the system normally used to study TIM15 effect on mtHsp70 solubility, differs from the one observed in yeast and therefore those results must always be interpreted with caution [10]. A clear example of this was the recent observation that the solubility of mtHsp70 coexpressed with Hep mutated in a histidine residue (H107) proposed to be essential for Hep–mtHsp70 interaction was not different from the one observed with WT Hep [12]. Moreover, in vitro assays using crosslinking agents [8] or gel filtration [7], although informative, are not suitable to follow the aggregation process of mtHsp70, due to their inherent short incubation times.

In order to study the effect of $Zn^{2+}$ on TIM15 chaperoning function we used an in vitro assay based on Thioflavin T (ThT) fluorescence to monitor protein aggregation. Despite that ThT is considered a specific amyloid dye, it also binds with moderate to high affinity to other beta-sheet enriched aggregates [32,33]. As expected, purified Ssc1 (mtHsp70) (10 μM) aggregates when incubated at 30 °C (see Fig. S1 for transmission electronic microscopy images), resulting in a time-dependent increase in ThT fluorescence (Fig. 1) and a calculated aggregation rate of $0.00225 \pm 0.0004$ $min^{-1}$. A large attenuation in mtHsp70 aggregation was observed upon addition of an equimolar concentration of purified TIM15c, reflected in a significant reduction in the aggregation rate ($0.00145 \pm 0.0005$ $min^{-1}$). This TIM15c solubilizing effect is abolished in the presence of EDTA (aggregation rate of $0.00230 \pm 0.0001$ $min^{-1}$) where TIM15c exists in its apo state (Fig. 1). TIM15c is a trypsin-resistant core of TIM15 (residues 64–159) that has been structurally characterized and can functionally replace TIM15 in yeast cells [9]. We studied the aggregation in nucleotide free conditions because the interaction between TIM15 and mtHsp70 has been shown to be stronger in the absence of nucleotides [7,8,11] and the addition of EDTA, used to remove and exclude any $Zn^{2+}$ coordination by TIM15c, would also prevent nucleotide coordination due to $Mg^{2+}$ chelation [9]. As a control, and because TIM15c in the absence of $Zn^{2+}$ aggregates at 60 °C, we included an assay with TIM15c plus EDTA, for

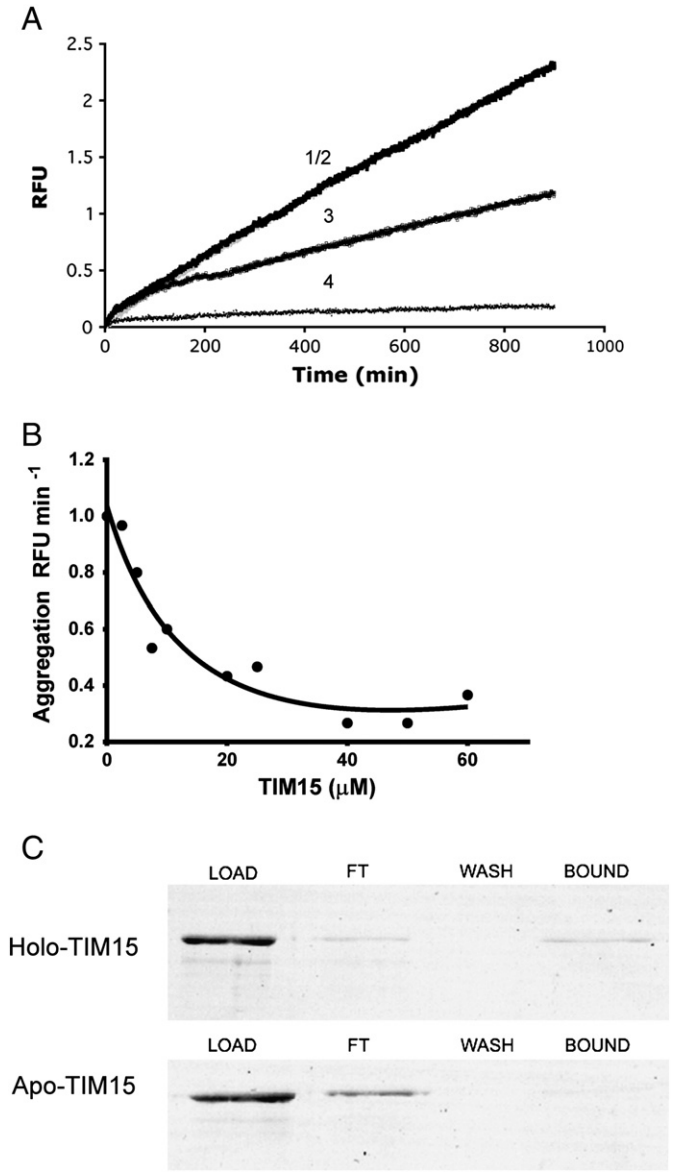


**Fig. 1.** Holo TIM15 binds to Ssc1 and is able to prevent its aggregation. A, Ssc1 alone (curve 1, black) or in the presence of equimolar concentration of apo-TIM15 (curve 2, gray) or holo-TIM15 (curve 3) was incubated at 30 °C in the presence of 25 μM of thioflavin T. Apo TIM15 was used as a control (curve 4) and fluorescence was measured using excitation 450 nm and emission 480 nm. Rates were calculated considering the linear part of the curves. B, Ssc1 in the presence of different concentrations of holo-TIM15 was incubated at 30 °C in the presence of 25 μM of thioflavin T. Aggregation rates were calculated as above, plotted as a function of TIM15c concentration and fitted to a single site binding equation. C, GST-TIM15 (1 μM) was incubated with nucleotide free Ssc1 (1 μM) and glutathione sepharose in the presence or absence of 1 mM EDTA (Load). The resin was washed with or without EDTA and the flow trough (FT) and washed resins were collected. The protein associated to TIM15 (Bound) was eluted with glutathione 20 mM.

which no significant aggregation at 30 °C was observed (Fig. 1A). To our knowledge, these results are the first direct in vitro evidence that TIM15 without the aid of any cellular *E. coli* or yeast cofactor prevents mtHsp70 aggregation and that $Zn^{2+}$ coordination is fundamental for this effect. Curiously, while TIM15c can reduce the rate of aggregation in a concentration dependent manner it cannot abolish it in vitro. As shown in Fig. 1B, even at saturating TIM15c concentrations ($K_D = 17$ μM) we can still observe mtHsp70 aggregation.

Next, we analyzed if $Zn^{2+}$ coordination affects the binding of TIM15 to mtHsp70. In order to test this interaction, a previously reported fusion protein between glutathione S-transferase (GST) and TIM15 [9] was used and incubated with mtHsp70 with or without EDTA and subjected to pull-down assays by using glutathione–sepharose beads. When the bound fractions were eluted with glutathione 20 mM we observe that mtHsp70 binds to the GST-TIM15 fusion in the presence of $Zn^{2+}$ but when EDTA is also present that interaction is strongly attenuated (Fig. 1C). These results are in agreement with recent observations by Zhai and coworkers, who using truncations of the Hep demonstrated that the $Zn^{2+}$ binding domain (ZBD) is fundamental for Hep–mtHsp70 interaction [31].

The solution structure of TIM15 in the $Zn^{2+}$ loaded state was recently described [9]. The protein consists of two subdomains, an N-terminal subdomain made up of a pair of two-stranded β-sheets that coordinate $Zn^{2+}$, whereas the C-terminal domain contains a mixture of α-helix, β-sheet and random coil [9]. Contrasting with the $Zn^{2+}$ state, the reduced chemical-shift dispersion in the NH resonances suggests that in its apo state TIM15 exists mainly in an unfolded state [9]. This is a common characteristic of $Zn^{2+}$ finger proteins that normally do not possess a defined apo structure [34] and probably represents the state in which TIM15 is translocated into the mitochondrial matrix. Indeed, we confirmed this feature using different biophysical techniques. While the CD spectrum obtained in the presence of 50 μM $Zn^{2+}$ is characteristic of a folded protein, containing two minima at ~207 and 220 nm consistent with a mixed α-helix and β-sheet secondary structure [9,31], the spectrum obtained in the presence of EDTA is indicative of an overall unstructured protein (Fig. 2A) and is similar to the one recently reported for the truncated protein not containing the ZBD [31]. ANS is an extrinsic fluorophore that is weakly fluorescent in aqueous environment but fluoresces strongly when located in a hydrophobic environment. Using ANS, we observed an increase in the probe fluorescence associated with TIM15 folding in the presence of $Zn^{2+}$ (Fig. 2B), consistent with the formation of an ordered core in which certain hydrophobic residues form clusters that are still significantly exposed to solvent [9,35]. Curiously the change in intensity was not coupled to a significant blue shift and this may be indicative that some residual hydrophobic packing exists already in the absence of the metal. The $Zn^{2+}$ promoted conformational change could also be confirmed by intrinsic tyrosine fluorescence, which was observed to increase in the presence of the metal ion (Fig. 2C). TIM15c contains 2 Tyr residues (Y91 and Y157, TIM15 numbering). In the native state, Y157 is highly exposed to solvent (87.5% of the area) and displays high mobility; therefore its fluorescence emission is not expected to change significantly upon folding. In contrast, Y91 forms a hydrophobic cluster with M86, V96, and A110, which are totally buried in the native conformation, hiding 72.4% of its area from the solvent, likely accounting for the observed differences in fluorescence between the holo and apo-forms. The shift from a loosely folded to a folded protein in the presence of $Zn^{2+}$ could also be confirmed by limited proteolysis, frequently used to assess the flexibility of protein regions, as unfolded protein regions are generally more accessible to the protease active site [34]. In agreement with the spectroscopy data, proteinase K digestion clearly demonstrates that relative to the $Zn^{2+}$ loaded state the apo state is more susceptible to proteolysis (Fig. 2D).

It is clear from the above data that in order to be functional as a chaperone TIM15 must previously fold while in the mitochondrial matrix, but this process has so far not been characterized. One important question is how much time it would take for TIM15c to gain its fold once it is translocated. In order to study the kinetics of TIM15 folding we took advantage of the above-described increase in ANS fluorescence upon $Zn^{2+}$ coordination. When a mixture containing TIM15c in EDTA was mixed with an excess of $Zn^{2+}$ a single time resolvable fluorescence intensity increase was observed (Fig. 3). The resolved kinetic phase could be fitted with a single exponential function rendering an estimated folding rate ($K_{obs}$) of 5.44 $s^{-1}$. Interestingly, the rate constant observed for TIM15c is in the range of the constants observed for short zinc-binding peptides [36,37], implying that the folding of this protein

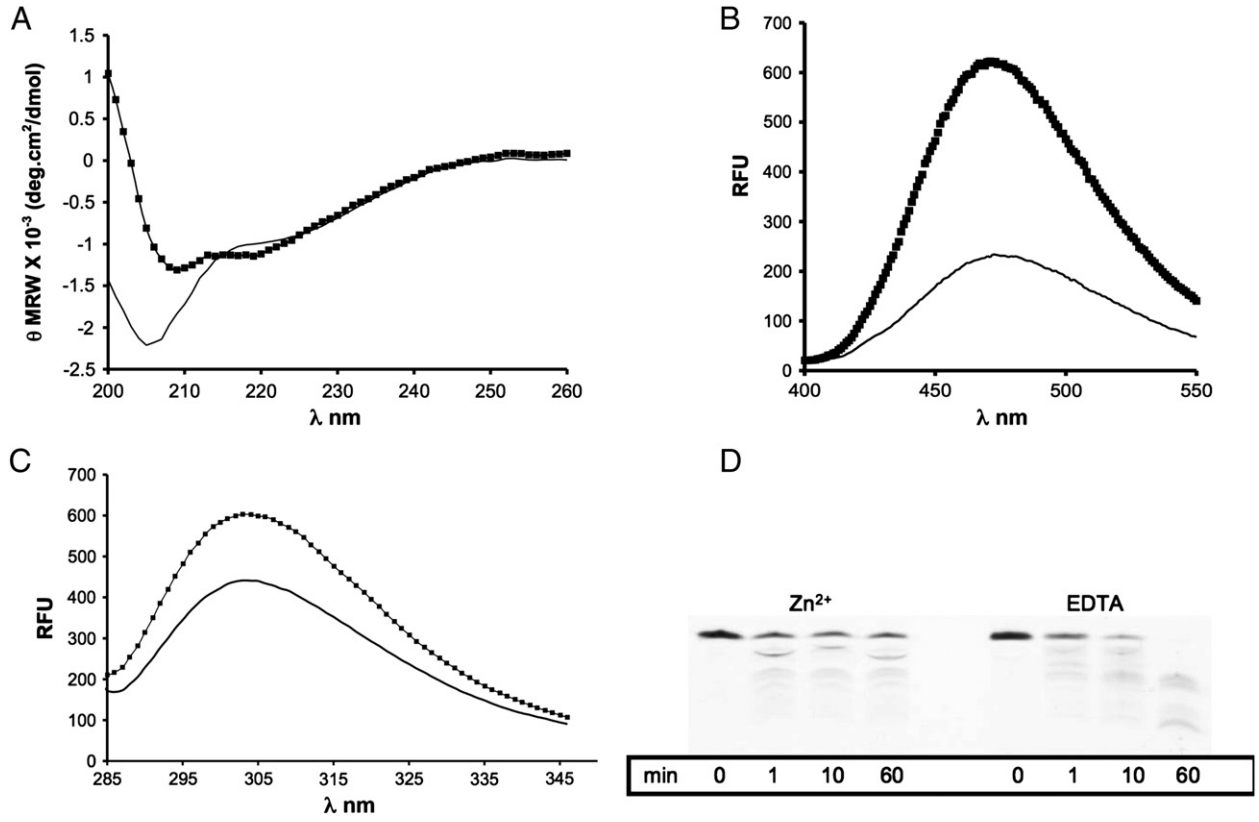


**Fig. 2.** $Zn^{2+}$ binding results in TIM15 folding. A, The removal of $Zn^{2+}$ with the addition of EDTA results in a profound modification in the CD spectra of TIM15c. While the holo-TIM15 contains features of a properly folded protein (squares), apo-TIM15 does not (line). B, The existence of a hydrophobic core is characteristic of a folded protein and can be monitored with the use of sensitive fluorescent probes. Reflecting the existence of a defined but still significantly exposed hydrophobic core, ANS fluorescence is more intense in the presence of the holo-TIM15 (squares) compared to apo-TIM15 (line). C, Tyrosine fluorescence is affected by $Zn^{2+}$ coordination reflected in a higher aminoacid quantum yield in holo-TIM15 (squares) compared to apo-TIM15 (line). D, Restricted proteolysis can be used to monitor protein folding since unfolded proteins are more susceptible to proteolysis. Proteinase K was added to TIM15 in the presence of EDTA or $Zn^{2+}$ and in agreement with the previous data digestion with proteinase K is faster with apo-TIM15 (EDTA) relative to the folded holo-TIM15 $Zn^{2+}$.

occurs in a time scale comparable to a minimal $Zn^{2+}$ finger domain peptide [34,36].

We proceeded in characterizing thermodynamically the TIM15/$Zn^{2+}$ interaction using isothermal titration calorimetry. The results are summarized in Table 1 and Fig. 4. The interaction is characterized by a moderate affinity ($K_d$ = 0.4 μM at 25 °C and 30 °C), close to those estimated for TIM9 ($K_d$ = 0.2 μM) and TIM10 ($K_d$ = 0.1 μM) at 30 °C [38]. At this temperature the interaction displays favorable enthalpic and entropic contributions ($\Delta H = -1.9$ kcal/mol, $-T\Delta S = -6.9$ kcal/mol). The most striking feature of the reaction is the remarkable temperature dependency of the thermodynamic parameters (enthalpy and entropy), with a heat capacity change upon binding $\Delta C_P = -1.2$ kcal/K·mol, yet maintaining a constant binding Gibbs energy (ΔG around −9 kcal/mol), a perfect example of enthalpy–entropy compensation. The experimentally determined $\Delta C_P$ for $Zn^{2+}$ binding to TIM15 is equal to that calculated for TIM15 folding obtained from the structural parameterization of the protein folding/unfolding energetics based on changes in solvent accessible (polar and non-polar) surface area [39], considering the NMR structure for the native state (PDB code: 2E2Z) and using ProtSA software for modeling the unfolded state [40]. The changes in polar and non-polar solvent accessible surface areas for TIM15c folding are −1002.6 Å$^2$ and −3519.5 Å$^2$, respectively, and the folding heat capacity calculated from these values is −1.3 kcal/K·mol. The agreement between the experimentally determined heat capacity change for $Zn^{2+}$ binding to TIM15 and the calculated heat capacity change for TIM15 folding suggests that, as it occurs in other $Zn^{2+}$ binding proteins, metal coordination is tightly coupled to protein folding [17,41,42]. Probably, the affinity of $Zn^{2+}$ binding to TIM15 is affected because $Zn^{2+}$ binding to TIM15 is strongly coupled to the folding of the protein with a significant energetic penalty from the folding step. The folding induced by $Zn^{2+}$ also affects the thermal stability of the protein as confirmed using DSC, where $Zn^{2+}$-bound TIM15c showed an unfolding transition with a $T_m$ of 72 °C and an unfolding enthalpy of 45 kcal/mol while $Zn^{2+}$-free TIM15c did not

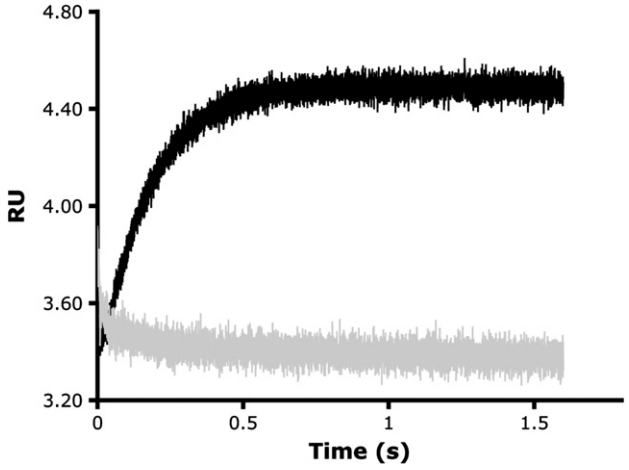


**Fig. 3.** Kinetics of TIM15 folding. The increase in ANS fluorescence with the addition of $Zn^{2+}$ to TIM15 was used to evaluate the protein folding rate. Using a stopped-flow apparatus, a mixture of ANS and saturating $Zn^{2+}$ was rapidly mixed with a solution containing apo-TIM15 (black curve) resulting in the expected increase in ANS fluorescence. The increase in fluorescence could be fitted to a single exponential with a rate of 5.44 $s^{-1}$. A control run with no $Zn^{2+}$ added was also performed (gray curve).

**Table 1**
Thermodynamic parameters for $Zn^{2+}$ binding to TIM15 at pH 4.5, sodium chloride 50 mM, DTT 1 mM.

| T (°C) | $K_a$ ($\times 10^6$ $M^{-1}$) | ΔG (kcal/mol) | ΔH (kcal/mol) | −TΔS (kcal/mol) | $\Delta C_P$ (kcal/K·mol) |
|---|---|---|---|---|---|
| 15 | 4.9 | −8.8 | 12.0 | −20.8 | −1.2 |
| 20 | 4.2 | −8.9 | 4.7 | −13.6 | |
| 25 | 2.6 | −8.8 | −1.9 | −6.9 | |
| 30 | 2.5 | −8.9 | −6.5 | −2.4 | |

$K_a$ is the association constant ($=1/K_d$).
$\Delta C_P$ is obtained as the temperature derivative of the binding enthalpy ($=(\partial\Delta H/\partial T)_P$).
Typical relative errors are 20% ($K_a$), 5% (ΔG, ΔH, −TΔS), and 10% ($\Delta C_P$).

exhibit any unfolding transition (Fig. S2) and, in addition, severe aggregation occurred upon denaturation at high temperature (above 60 °C).

Since the structure of the apo state cannot be accessed experimentally [9] and to better disclose, at the molecular level, the effects induced by $Zn^{2+}$ on the structure and dynamics of TIM15, 100 ns molecular dynamics (MD) simulations of the $Zn^{2+}$-bound (holo) and $Zn^{2+}$-free (apo) TIM15c were carried out. In the MD framework here provided, unfolding events cannot be followed, but relevant insights on how the absence of the $Zn^{2+}$ ion can affect protein dynamics and native intramolecular interactions can be obtained, as shown for other metallo-proteins [43–46].

First, to identify the protein region most affected by the absence of the metal ion, principal component analysis (PCA) of the MD ensemble of both the apo- and holo-forms was employed. The PCA applied to the MD simulations allows generating appropriate collective coordinates that capture the most relevant motions of the protein MD ensemble [29,47]. In particular, the motions described by the first principal component, which account for more than the 40% of the total variance, clearly show differences in the holo- and apo-TIM15c (Fig. 5). In the native holo-TIM15c, the major displacement is observed in the loop region between the residues 131 and 136 (Fig. 5A), in agreement with experimental NMR data indicating that this segment is highly flexible in solution. The rest of the protein structure is characterized by low fluctuations. In particular, the loops in the regions 72–83 and 100–106, in which the coordinating cysteines for $Zn^{2+}$ are located, feature reciprocal well-concerted and organized motions in holo-TIM15c (Fig. 5A). On the contrary, in the apo-form, a higher displacement can be observed across the whole structure and the loop regions of the metal binding site lose their concerted motions (Fig. 5B). Also the motions of the interaction interface for mtHsp70 in the concave face of TIM15, which include the residues D111, H107 and R106 [9,12] are strongly affected by the absence of $Zn^{2+}$. The effects are also transmitted long-range to the regions 112–122, to which some of the residues that face H107 and R106 belong, as well as the C-terminal regions. On the opposite, the 131–136 loop, which was highly mobile in the holo-variant (Fig. 5A), has a decreased flexibility in the apo-form (Fig. 5B), suggesting a long-range effect exerted by the $Zn^{2+}$ ion and transmitted to this loop in the holo-protein. Interestingly, a deletion of the 133–137 stretch impairs yeast cell growth, mitochondrial protein import and the TIM15-dependent suppression of mtHsp70 aggregation [9], pointing out a relevant functional role for the 131–136 loop.

To better identify the effects induced by $Zn^{2+}$ on protein dynamics, the correlated and anti-correlated motions were calculated in the apo- and holo-forms by the analysis of dynamical cross-correlation matrices (DCCM) (Fig. 5C–D). DCCM were calculated both as average matrices on different timescales, i.e. averages of matrices calculated with time-windows of 1 ns, 5 ns and 10 ns. The general view, emerging from the DCCM analyses, is that in the native $Zn^{2+}$-bound TIM15c dynamics there is a network of well-defined anti-correlated motions (Fig. 5C in blue) between the two loops bearing the cysteine residues for $Zn^{2+}$ coordination, indicating the tendency of these two regions to approach each other due to the presence of the $Zn^{2+}$ ion in the binding pocket (Fig. 5C). These anti-correlations, together with another group of positively correlated motions (Fig. 5C), also involve the key residues for mtHsp70 interaction [9]. Moreover, a group of highly positively correlated residues can be identified, involving the internal β-sheet, D111, conserved among TIM15 homologs in various organisms, and the loop in which the aspartate is located (Fig. 5C). In the apo-form, the anti-correlated motions governing the $Zn^{2+}$-coordinating loops are completely lost and also the other networks of correlation are affected (Fig. 5D), resulting in anti-correlated motions on the opposite part of the protein.

In light of the effects induced by $Zn^{2+}$ removal on native TIM15c protein dynamics, also the networks of intramolecular interactions, both electrostatic (salt bridges, aromatic and cation–PI interactions) and hydrophobic interactions, were calculated from the MD ensembles,

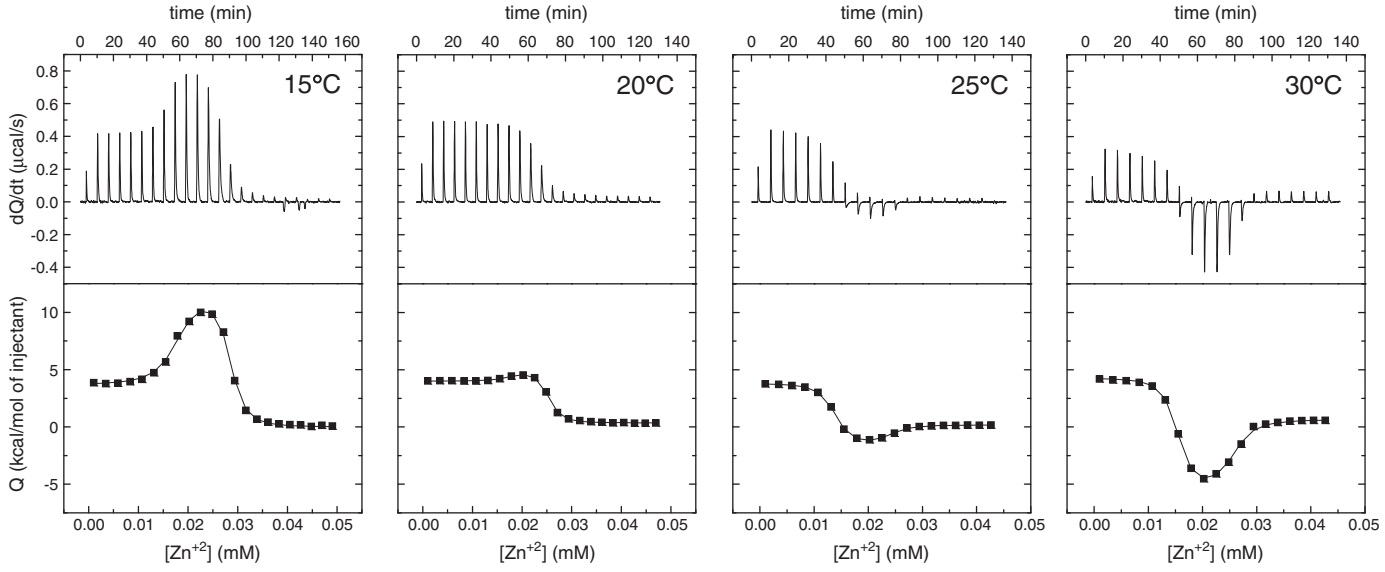


**Fig. 4.** Calorimetric titrations for $Zn^{2+}$ binding to TIM15. Experiments were performed at different temperatures in order to determine the heat capacity change upon binding. The thermograms (thermal power vs. time) are shown in the upper plots and the binding isotherms (heat vs. concentration) in the lower plots. Biphasic titrations are observed for the binding of $Zn^{2+}$ to excess EDTA (first event) and the binding of $Zn^{2+}$ to TIM15 (second event). A marked temperature dependency for the binding of $Zn^{2+}$ to TIM15 is observed.

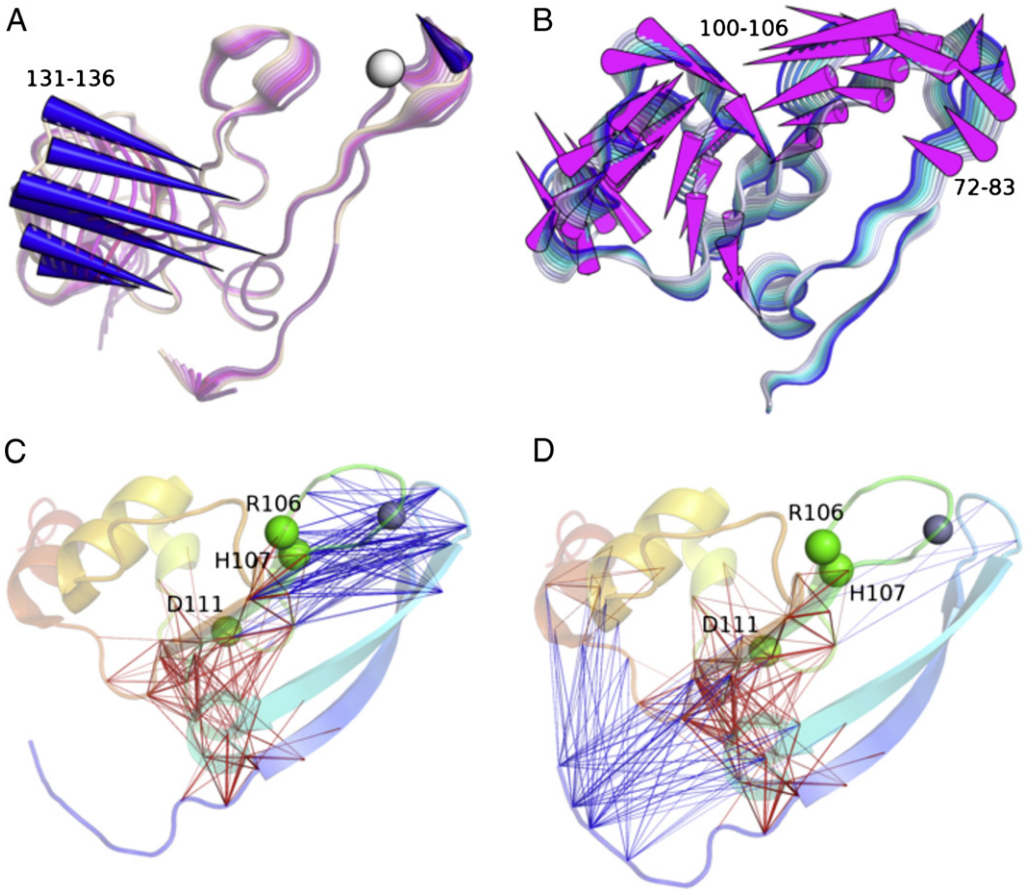


**Fig. 5.** Dominant motions in the MD simulations of the holo- and apo-TIM15c forms using Principal Component Analysis (PCA) (A–B) and distribution of the networks of correlated motions during dynamics (C–D). Porcupine plot of the displacement along the first principal component for the holo-TIM15c (A, in blue) and apo-TIM15 (B, in magenta) simulations. The projection of the simulation frames along the first principal component are indicated as different shades of magenta and blue, for the holo- and apo-TIM15c, respectively. The position of the $Zn^{2+}$ metal ion is indicated as a reference in the holo-TIM15c (A). C–D) The networks of more significant correlated (red) and anti-correlated (blue) residues are indicated as sticks in holo-TIM15c (C) and apo-TIM15c (D). D111, R106 and H107 and $Zn^{2+}$ (position of the $Zn^{2+}$ is taken from the holo-TIM15c structure as a reference) are indicated as spheres and the 3D structure is colored from blue to red from the N- to the C-terminal extremities. (For interpretation of the references to color in this figure, the reader is referred to the web version of this article.)

along their persistence (Fig. 6). There are no significant aromatic or amino–aromatic interactions in the native holo-TIM15c dynamics beside N80–F143 (68% of the frames) and K114–Y157 (65% of the frames) that is related to conformational changes of the C-terminal extremity of the domain that allow Y157 to approach to K114 and are not observed in the apo-form. Salt bridge interactions are particularly affected by the $Zn^{2+}$ absence (Fig. 6A–B) as they are the native network of hydrophobic contacts. Since MD simulations were carried out on an ns timescale, they do not allow the assessment of the changes of hydrophobic interactions in the protein core in atomic detail. However, it is worth mentioning that hydrophobic interactions in the regions in proximity to the $Zn^{2+}$-binding loops, as well as in distal regions are altered and display lower persistence. The total number of hydrophobic interactions is 1.6 fold lower in the apo-form than in the holo-protein. The hydrophobic cluster containing the conformation-sensitive Y91 is almost lost in the apo-simulations, whereas it is maintained in the native MD simulation. The interactions within this hydrophobic cluster involving Y91, V96 and M86 are absent or at a very low persistence (<20–25%) in the apo-TIM15c simulations (Fig. S3). Not only individual salt bridges are modified in apo-form, but their perturbation alters the distribution of these networks and their organization into clusters of spatial proximity. In fact, the native holo-TIM15c features one main cluster of spatial proximity including different salt bridges (accounting 16 residues), which from the vicinity of the metal ion binding site connect different protein regions (Fig. 6A). This cluster also includes D111 and R106, lying at the mtHsp70 interaction interface. D111 interacts with K114, whereas R106 is involved in a tridentate network with D140 and D137 at the base of the 131–136 loop (Fig. 6A). In fact, this tridentate salt bridge network on one side and the amino–aromatic interaction between N130 and F143 on the other side act stabilizing the hinges of the unstructured, but biologically relevant 130–139 loop. Removal of $Zn^{2+}$ causes a disruption of the main cluster of native salt bridges and an increase in the number of smaller and few populated clusters (Fig. 6B), in agreement with the previously discussed higher flexibility of the apo-form. In particular, R106 loses the electrostatic interaction with D140 and the N130 and F143 interaction losses persistence, causing a loss of the proper hinges for the concerted motion of the 131–139 loop. Moreover, also the native-like salt bridge between K68 and E142, which concurs to the proper reciprocal parallel orientation in the two β-sheets in TIM15c which is lost in the apo-form and replaced by non-native interactions with the N-terminal residues K66 and D65 (Fig. 6B).

To complete the picture provided by the MD comparative approach, the paths of communications between the $Zn^{2+}$-binding site and the rest of the protein structures were calculated to identify the regions on which the $Zn^{2+}$ ion can exert long-range effects (Fig. 7, Table 1S in the Supplementary materials). The paths were calculated employing the PSN-DCCM approach, which was successfully applied to other cases of study [25–27]. This approach for each pair of selected residues identifies the paths of shortest communication between the two residues that are more frequently explored during dynamics. In particular, we calculated the long-range paths mediated by

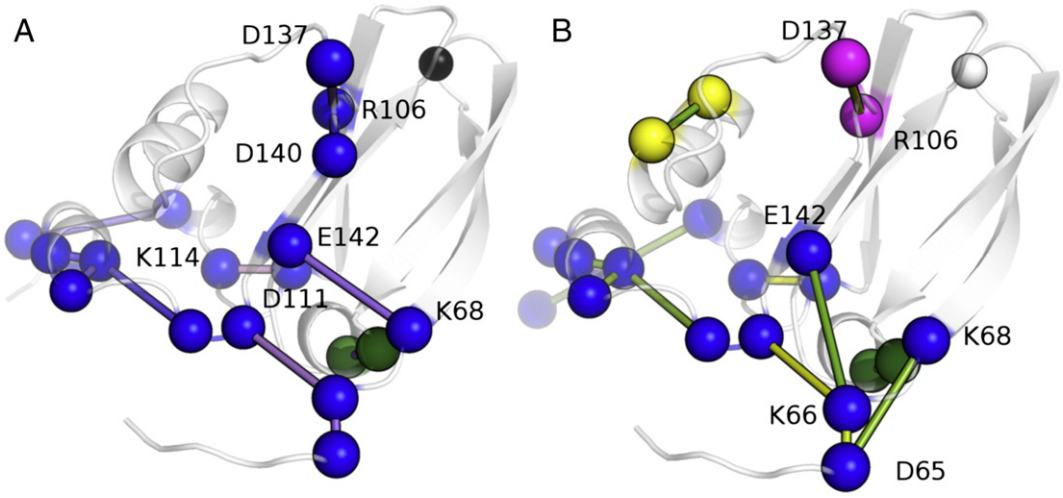


**Fig. 6.** Networks of salt bridges (A–B). The residues involved in salt bridges (A–B) or hydrophobic interactions (C–D) are shown as spheres, as well as the $Zn^{2+}$ ion. The position of the $Zn^{2+}$ ion is taken from the holo-TIM15c as a reference. The residues involved in salt bridges are with different colors, according to the cluster of spatial proximity to which they belong (clusters 1, 2, 3 and 4 in blue, dark green, yellow and magenta, respectively). The networks of salt bridges are represented as sticks of different shade of colors according to their persistence. The salt bridge networks are colored from blue to magenta, or yellow to green according to the decreasing persistence values in holo- (A) or apo-TIM15c (B), respectively. (For interpretation of the references to color in this figure, the reader is referred to the web version of this article.)

each of the $Zn^{2+}$-coordinating cysteines with the rest of the protein structure. It turns out that C75 and specially C100 have a pivotal role in mediating communication to different protein regions, including the interface for mtHsp70 interaction (Fig. 7, Table 1S). In particular, C75 and C100 are long-range connected to H107 and D111, respectively, whereas R106 is an important intermediate residue in several communication paths mediated by C100 to other protein regions. The perturbations induced on this distal communication upon $Zn^{2+}$ removal were assessed comparing the PSN-DCCM paths of the native holo-TIM15c and the paths identified in apo-TIM15c MD simulations. It turns out a different distribution of the paths of intramolecular communication mediated by the $Zn^{2+}$ binding residues. These paths are lower in number than in the holo-TIM15 simulations (44 and 13 in the holo- and apo-form, respectively) and do not communicate with the residues in the region for mtHsp70 interaction (Table 1S).

## 4. Discussion

Mitochondrial protein import has been the focus of important studies that shed light on the mechanisms behind the complex trafficking of proteins into the different organelle compartments. One of the mechanisms that has been shown to be involved in this sorting is the folding trap, a process by which, protein folding inside different organelle retains (or traps) the protein due to the inability of the folded protein to cross membrane barriers [48]. Several different strategies are exploited to achieve protein folding, including oxidative folding (Mia40–Erv1 pathway) [49], folding induced by ligand binding [50], as occurs with cytochrome c, or metal coordination. In this latter case, the $Zn^{2+}$ finger motif, a structural element that depends solely upon the presence of a bound metal ion for proper folding turns to be particularly useful [34]. In this context, the transfer of

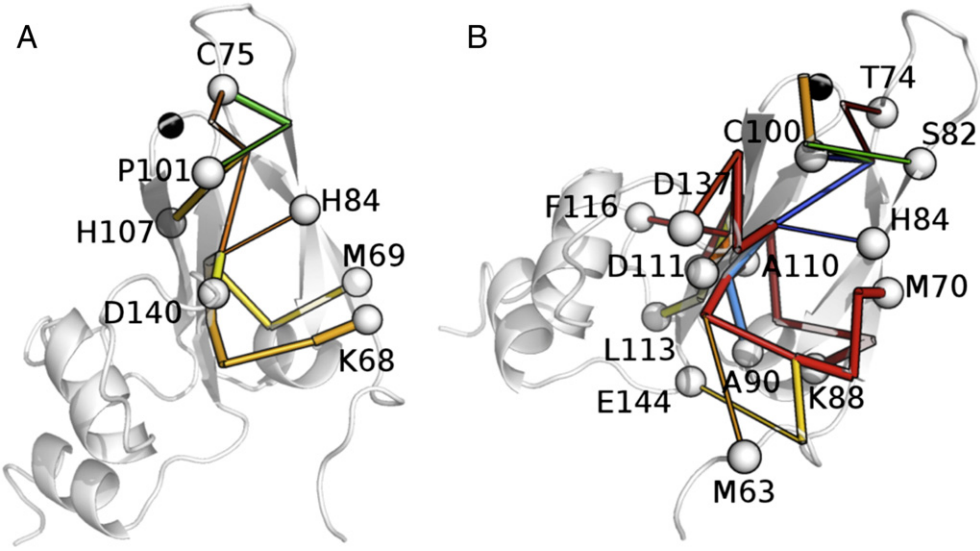


**Fig. 7.** Paths of long-range communication mediated by the $Zn^{2+}$-coordinating cysteine in holo-TIM15c, calculated according to the PSN-DCCM approach. The shortest and highest frequency (>10%) pathways of communication between the catalytic cysteines C75 (A) and C100 (B) are shown as sticks of size proportional to the intensity of the correlation. The catalytic cysteine used as root residue and the terminal residue of each communication path are shown as white spheres. The $Zn^{2+}$ ion is shown as a black sphere. Each communication path is shown with a different shade of color and in particular paths with frequency in the range of 10–20%, 20–30% and >30% are colored with different shades of yellow/red, green and blue, respectively. A list of the paths and the intermediate residues is provided in Table S1 as Supplementary materials. (For interpretation of the references to color in this figure, the reader is referred to the web version of this article.)

the protein to an organelle where the free pool of the ion is systematically higher, such as the mitochondrial matrix where high concentration of $Zn^{2+}$ and a large $Zn^{2+}$ binding proteome exist [51,52], would be an elegant way to couple folding and trapping of imported proteins inside the organelle. The data herein suggest that, in principle, a similar mechanism might work for TIM15.

Despite several studies having addressed the role of TIM15 as a mtHsp70 chaperone, none has focused on how its folding occurs or how it is coupled to this activity. Apart from the moderate binding affinity, the most remarkable feature of $Zn^{2+}$ binding to TIM15c is the large heat capacity change ($\Delta C_P = -1.2$ kcal/K·mol). Not surprisingly, this value is very close to the one calculated considering that the folding of TIM15c occurs from a strictly unfolded state, confirming the autonomous folding nature of $Zn^{2+}$ fingers. These data indicate that the apo form of TIM15 is in a conformation competent for crossing the organelle membranes.

Using stopped flow we demonstrated that in the presence of $Zn^{2+}$, the folding reaction is very fast and, apparently, does not involve the population of folding intermediates. However, it should be noted that the calculated folding rate is likely an overestimation of this occurring in vivo. The calculated $K_d$ (0.38 μM) to an estimated 0.6 μM free pool of $Zn^{2+}$ in the mitochondrial matrix [53,54] indicates that the used conditions probably do not reflect physiological conditions. Moreover as emphasized by Heinz and coworkers newly synthesized $Zn^{2+}$ proteins do not depend only on the pool of free $Zn^{2+}$ and will probably compete with other $Zn^{2+}$-loaded molecules [53]. In any case, our results do show that given the appropriate conditions TIM15 will independently fold. In this context, it is not clear, accepting that the current estimates for cytoplasmic $Zn^{2+}$ are not overestimated, how the folding of this protein is prevented in the cytoplasm. While lower than the mitochondrial matrix, the recently estimated pool of free $Zn^{2+}$ in the cytoplasm (0.18 μM) is still compatible with TIM15 folding in this compartment [54]. Contrary to other mitochondrial $Zn^{2+}$binding proteins, like TIM10 or TIM9, where the ion coordination has been shown to prevent cysteine oxidation and subsequent folding in the cytoplasm [55], it's unlikely that TIM15 $Zn^{2+}$ coordination will result in an increase in mitochondrial import, since, as we show here, the folded conformation is highly stable against unfolding and therefore not competent for translocation. Indeed, we failed to observe any significant spontaneous TIM15c cysteine oxidation, both under reducing and non-reducing conditions even after overnight incubation in the absence of $Zn^{2+}$ (Fig. S4). While recent studies have also shown that mitochondria are able to actively unfold proteins the unfolding/translocation efficiency is strictly related to the length and charge of the N-terminal pre-sequence and to the nature of the structure immediately after this signal [56]. For example, cytochrome b2 despite containing a tightly folded heme domain can, due to its 80 residues N-terminal presequence, be actively unfolded by the matrix mtHsp70 [57]. However, in the case of TIM15 the N-terminal sequence is considerably shorter, comprising 42 residues [8,9] and moreover the sequence following the N-terminal sequence is the $Zn^{2+}$ β-sheet domain shown by Wilcox et al. to dramatically hinder precursor translocation [56]. Clearly, the process of how TIM15c and other $Zn^{2+}$ finger proteins are presented to the mitochondria import machinery for translocation is an open topic for discussion but likely, whether by binding to chaperones or because the metal availability is tightly controlled, those proteins should be presented in the apo state. The presence of the $Zn^{2+}$ binding protein, Hot13, in the intermembrane space can be particularly relevant for an efficient traffic of these large groups of proteins as, a $Zn^{2+}$ free intermembrane space will prevent spontaneous folding before Tim23 translocation [58].

MD simulations confirm the crucial role of $Zn^{2+}$ in promoting a stable and native 3D structure and illustrate how this ion, through its coordinating cysteines (C75 and C110), mediate both local and long-range effects that allow communication between $Zn^{2+}$ and chaperone binding motifs. The stabilizing effects of the ion metal are transmitted in a well-orchestrate manner to the residues located at the interface for the interaction with mtHsp70, in particular to R106, D111 and H107, as well the loop 131–136, in agreement with mutagenesis data and the experimental evidence of a $Zn^{2+}$-dependent interactions with the chaperone [9]. A subset of other relevant residues for which the network of native interactions and dynamic properties are altered by metal ion depletion is suggested by the MD simulations, and will be the subject of future experimental investigations.

Moreover, the observed differences between the apo- and holo-variants in MD simulations suggest that in the absence of the metal ion, the N-terminal domain, where the metal binding resides, is the first site to unfold. The unfolding of the N-terminal domain is likely incompatible with the presence of a stable tertiary conformation in the rest of the protein, since most of TIM15 stable intramolecular interactions seem to depend on the presence of the $Zn^{2+}$ ion and on the reciprocal orientation of the two $Zn^{2+}$-coordinating loops. The conformational defects caused by metal ion loss are transmitted to the interaction interface for mtHsp70 and, through long-range effects, to the C-terminal end, since we observed in the apo-MD simulations an alteration of the native interactions involving the C-terminal residues, as in the case of Y157. MD simulations suggest that the apo-form might retain a certain degree of hydrophobic packing. However, in agreement with intrinsic and ANS fluorescence experiments, the hydrophobic interactions in this state are likely different from those sustaining the native, stable and well-defined hydrophobic core in the holo-form. In this way, the native cluster involving Y91, M86, V96 and A110 is clearly less persistent in the apo-MD ensemble and becomes replaced by other less stable interactions, which likely lead to the formation of a less compact ensemble.

Overall, the combination of experimental and computational approaches presented here provide an integrated structural, kinetic and thermodynamic view of the folding of a mitochondrial zinc finger protein, which might be relevant to understand the organelle import of proteins sharing this fold.

## Acknowledgements

H.F. is supported by a post doctoral fellowship (SFRH/BPD/76123/2011) from Fundação para a Ciência e Tecnologia, Portugal. Work in our lab is supported by grants BFU2010-14901 from Ministerio de Ciencia e Innovacion (Spain), and 2009-SGR-760 and 2009-CTP-00004 from AGAUR (Generalitat de Catalunya). S.V. has been granted an ICREA Academia award (ICREA). E.P. has been granted by a Standard HPC Grant 2011 from CASPUR (Consorzio interuniversitario per le Applicazioni di Supercalcolo Per Università e Ricerca) and by the HPC-EUROPA2 project with the support of the European Commission – Capacities Area – Research Infrastructure. A.V.C. was supported by grant BFU2010-19451 from the Ministerio de Ciencia e Innovacion (Spain).

## Appendix A. Supplementary data

Supplementary data to this article can be found online at http://dx.doi.org/10.1016/j.bbagen.2012.10.002.

## References

[1] W. Neupert, J.M. Herrmann, Translocation of proteins into mitochondria, Annu. Rev. Biochem. 76 (2007) 723–749.
[2] J.C. Young, N.J. Hoogenraad, F.U. Hartl, Molecular chaperones Hsp90 and Hsp70 deliver preproteins to the mitochondrial import receptor Tom70, Cell 112 (2003) 41–50.
[3] A. Chacinska, C.M. Koehler, D. Milenkovic, T. Lithgow, N. Pfanner, Importing mitochondrial proteins: machineries and mechanisms, Cell 138 (2009) 628–644.
[4] F.N. Vogtle, S. Wortelkamp, R.P. Zahedi, D. Becker, C. Leidhold, K. Gevaert, J. Kellermann, W. Voos, A. Sickmann, N. Pfanner, C. Meisinger, Global analysis of the mitochondrial N-proteome identifies a processing peptidase critical for protein stability, Cell 139 (2009) 428–439.
[5] H. Yamamoto, T. Momose, Y. Yatsukawa, C. Ohshima, D. Ishikawa, T. Sato, Y. Tamura, Y. Ohwa, T. Endo, Identification of a novel member of yeast mitochondrial

Hsp70-associated motor and chaperone proteins that facilitates protein translocation across the inner membrane, FEBS Lett. 579 (2005) 507–511.
[6] L. Burri, K. Vascotto, S. Fredersdorf, R. Tiedt, M.N. Hall, T. Lithgow, Zim17, a novel zinc finger protein essential for protein import into mitochondria, J. Biol. Chem. 279 (2004) 50243–50249.
[7] P. Zhai, C. Stanworth, S. Liu, J.J. Silberg, The human escort protein hep binds to the ATPase domain of mitochondrial Hsp70 and regulates ATP hydrolysis, J. Biol. Chem. 283 (2008) 26098–26106.
[8] M. Sichting, D. Mokranjac, A. Azem, W. Neupert, K. Hell, Maintenance of structure and function of mitochondrial Hsp70 chaperones requires the chaperone Hep1, EMBO J. 24 (2005) 1046–1056.
[9] T. Momose, C. Ohshima, M. Maeda, T. Endo, Structural basis of functional cooperation of Tim15/Zim17 with yeast mitochondrial Hsp70, EMBO Rep. 8 (2007) 664–670.
[10] M. Blamowska, M. Sichting, K. Mapa, D. Mokranjac, W. Neupert, K. Hell, ATPase domain and interdomain linker play a key role in aggregation of mitochondrial Hsp70 chaperone Ssc1, J. Biol. Chem. 285 (2009) 4423–4431.
[11] A.V. Goswami, B. Chittoor, P. D'Silva, Understanding the functional interplay between mammalian mitochondrial Hsp70 chaperone machine components, J. Biol. Chem. 285 (2010) 19472–19482.
[12] P. Zhai, M.T. Vu, K.G. Hoff, J.J. Silberg, A conserved histidine in human DNLZ/HEP is required for stimulation of HSPA9 ATPase activity, Biochem. Biophys. Res. Commun. 408 (2011) 589–594.
[13] L.K. Sanjuán Szklarz, B. Guiard, M. Rissler, N. Wiedemann, V. Kozjak, M. van der Laan, C. Lohaus, K. Marcus, H.E. Meyer, A. Chacinska, N. Pfanner, C. Meisinger, Inactivation of the mitochondrial heat shock protein zim17 leads to aggregation of matrix hsp70s followed by pleiotropic effects on morphology and protein biogenesis, J. Mol. Biol. 351 (2005) 206–218.
[14] M.D. Díaz de la Loza, M. Gallardo, M.L. García-Rubio, A. Izquierdo, E. Herrero, A. Aguilera, R.E. Wellinger, Zim17/Tim15 links mitochondrial iron–sulfur cluster biosynthesis to nuclear genome stability, Nucleic Acids Res. (2011) 1–14.
[15] R.N. Goldberg, N. Kishore, R.M. Lennen, Thermodynamic quantities for the ionization reactions of buffers, J. Phys. Chem. Ref. Data 31 (2002) 231–370.
[16] X. Arias-Moreno, S. Cuesta-Lopez, O. Millet, J. Sancho, A. Velazquez-Campoy, Thermodynamics of protein–cation interaction: $Ca^{+2}$ and $Mg^{+2}$ binding to the fifth binding module of the LDL receptor, Proteins 78 (2010) 950–961.
[17] O. Abian, J.L. Neira, A. Velazquez-Campoy, Thermodynamics of zinc binding to hepatitis C virus NS3 protease: a folding by binding event, Proteins 77 (2009) 624–636.
[18] X. Arias-Moreno, A. Velazquez-Campoy, J.C. Rodríguez, M. Pocoví, J. Sancho, Mechanism of low density lipoprotein (LDL) release in the endosome, J. Biol. Chem. 283 (2008) 22670–22679.
[19] K. Lindorff-Larsen, S. Piana, K. Palmo, P. Maragakis, J.L. Klepeis, R.O. Dror, D.E. Shaw, Improved side-chain torsion potentials for the Amber ff99SB protein force field, Proteins 78 (2010) 1950–1958.
[20] D.C. Bas, D.M. Rogers, J.H. Jensen, Very fast prediction and rationalization of pKa values for protein–ligand complexes, Proteins 73 (2008) 765–783.
[21] B. Hess, H. Bekker, H.J.C. Berendsen, J.G.E.M. Fraaije, LINCS: a linear constraint solver for molecular simulations, J. Comput. Chem. 18 (1997) 1463–1472.
[22] T. Darden, D. York, L. Pedersen, Particle mesh Ewald: an N·log(N) method for Ewald sums in large systems, J. Chem. Phys. 98 (1993) 10089–10092.
[23] P.H. Hunenberger, A.E. Mark, W.F. van Gunsteren, Fluctuation and cross-correlation analysis of protein motions observed in nanosecond molecular dynamics simulations, J. Mol. Biol. 252 (1995) 492–503.
[24] S. Vishveshwara, A. Ghosh, P. Hansia, Intra and inter-molecular communications through protein structure network, Curr. Protein Pept. Sci. 10 (2009) 146–160.
[25] A. Ghosh, S. Vishveshwara, A study of communication pathways in methionyl–tRNA synthetase by molecular dynamics simulations and structure network analysis, Proc. Natl. Acad. Sci. U.S.A. 104 (2007) 15711–15716.
[26] A. Ghosh, R. Sakaguchi, C. Liu, S. Vishveshwara, Y.-M. Hou, Allosteric communication in cysteinyl tRNA synthetase, J. Biol. Chem. 286 (2011) 37721–37731.
[27] F. Fanelli, A. Felline, Dimerization and ligand binding affect the structure network of A2A adenosine receptor, Biochim. Biophys. Acta 1808 (2011) 1256–1266.
[28] M. Seeber, A. Felline, F. Raimondi, S. Muff, R. Friedman, F. Rao, A. Caflisch, F. Fanelli, Wordom: a user-friendly program for the analysis of molecular structures, trajectories, and free energy surfaces, J. Comput. Chem. 32 (2011) 1183–1194.
[29] A. Amadei, A.B. Linssen, H.J. Berendsen, Essential dynamics of proteins, Proteins 17 (1993) 412–425.
[30] M. Tiberti, E. Papaleo, Dynamic properties of extremophilic subtilisin-like serine-proteases, J. Struct. Biol. 174 (2011) 69–83.
[31] M.T. Vu, P. Zhai, J. Lee, C. Guerra, S. Liu, M.C. Gustin, J.J. Silberg, The DNLZ/HEP zinc-binding subdomain is critical for regulation of the mitochondrial chaperone HSPA9, Prot. Sci. 21 (2012) 258–267.
[32] M. Carrio, N. Gonzalez-Montalban, V.A. Villaverde, S. Ventura, Amyloid-like properties of bacterial inclusion bodies, J. Mol. Biol. 347 (2005) 1025–1037.
[33] L. Wang, D. Schubert, M.R. Sawaya, D. Eisenberg, R. Riek, Multidimensional structure–activity relationship of a protein in its aggregated states, Angew. Chem. Int. Ed Engl. 49 (2010) 3904–3908.
[34] A.D. Frankel, J.M. Berg, C.O. Pabo, Metal-dependent folding of a single zinc finger from transcription factor IIIA, Proc. Natl. Acad. Sci. U.S.A. 84 (1987) 4841–4845.
[35] H. Fraga, T.Q. Faria, F. Pinto, A. Almeida, R.M.M. Brito, A.M. Damas, FH8 — a small EF-hand protein from *Fasciola hepatica*, FEBS J. 277 (2010) 5072–5085.
[36] C.B. Anfinsen, E. Haber, M. Sela, F.H.J. White, The kinetics of formation of native ribonuclease during oxidation of the reduced polypeptide chain, Proc. Natl. Acad. Sci. U.S.A. 47 (1961) 1309–1314.
[37] J. Tang, S.-G. Kang, J.G. Saven, F. Gai, Characterization of the cofactor-induced folding mechanism of a zinc-binding peptide using computationally designed mutants, J. Mol. Biol. 389 (2009) 90–102.
[38] H. Lu, S. Allen, L. Wardleworth, P. Savory, K. Tokatlidis, Functional TIM10 chaperone assembly is redox-regulated in vivo, J. Biol. Chem. 279 (2004) 18952–18958.
[39] K.P. Murphy, E. Freire, Thermodynamics of structural stability and cooperative folding behavior in proteins, Adv. Protein Chem. 43 (1992) 313–361.
[40] J. Estrada, P. Bernado, M. Blackledge, J. Sancho, ProtSA: a web application for calculating sequence specific protein solvent accessibilities in the unfolded ensemble, BMC Bioinforma. 10 (2009) 104.
[41] X. Arias-Moreno, O. Abian, S. Vega, J. Sancho, A. Velazquez-Campoy, Protein–cation interactions: structural and thermodynamic aspects, Curr. Protein Pept. Sci. 12 (2011) 325–338.
[42] O. Abian, S. Vega, J.L. Neira, A. Velazquez-Campoy, Conformational stability of hepatitis C virus NS3 protease, Biophys. J. 99 (2010) 3811–3820.
[43] M.-M. Blum, J.C.-H. Chen, Structural characterization of the catalytic calcium-binding site in diisopropyl fluorophosphatase (DFPase) — comparison with related beta-propeller enzymes, Chem. Biol. Interact. 187 (2010) 373–379.
[44] G. Invernizzi, E. Papaleo, R. Grandori, L. De Gioia, M. Lotti, Relevance of metal ions for lipase stability: structural rearrangements induced in the Burkholderia glumae lipase by calcium depletion, J. Struct. Biol. 168 (2009) 562–570.
[45] M. Falconi, F. Oteri, F. Di Palma, S. Pandey, A. Battistoni, A. Desideri, Structural–dynamical investigation of the ZnuA histidine-rich loop: involvement in zinc management and transport, J. Comput. Aided Mol. Des. 25 (2011) 181–194.
[46] F. Ding, N.V. Dokholyan, Dynamical roles of metal ions and the disulfide bond in Cu, Zn superoxide dismutase folding and aggregation, Proc. Natl. Acad. Sci. U.S.A. 105 (2008) 19696–19701.
[47] P.I. Zhuravlev, C.K. Materese, G.A. Papoian, Deconstructing the native state: energy landscapes, function, and dynamics of globular proteins, J. Phys. Chem. 113 (2009) 8800–8812.
[48] T. Lutz, W. Neupert, J.M. Herrmann, Import of small Tim proteins into the mitochondrial intermembrane space, EMBO J. 22 (2003) 4400–4408.
[49] H. Fraga, S. Ventura, Protein oxidative folding in the intermembrane mitochondrial space: more than protein trafficking, Curr. Protein Pept. Sci. 13 (2012).
[50] J.M. Herrmann, J. Riemer, The intermembrane space of mitochondria, Antioxid. Redox Signal. 13 (2010) 1341–1358.
[51] F. Pierrel, P. Cobine, D. Winge, Metal ion availability in mitochondria, Biometals 20 (2007) 675–682.
[52] A. Atkinson, O. Khalimonchuk, P. Smith, H. Sabic, D. Eide, D.R. Winge, Mzm1 influences a labile pool of mitochondrial zinc important for respiratory function, J. Biol. Chem. 285 (2010) 19450–19459.
[53] U. Heinz, On the competition for available zinc, J. Biol. Chem. 280 (2004) 3197–3207.
[54] P.J. Dittmer, J.G. Miranda, J.A. Gorski, A.E. Palmer, Genetically encoded sensors to elucidate spatial distribution of cellular zinc, J. Biol. Chem. 284 (2009) 16289–16297.
[55] H. Lu, J. Woodburn, Zinc binding stabilizes mitochondrial Tim10 in a reduced and import-competent state kinetically, J. Mol. Biol. 353 (2005) 897–910.
[56] A.J. Wilcox, J. Choy, C. Bustamante, A. Matouschek, Effect of protein structure on mitochondrial import, Proc. Natl. Acad. Sci. U.S.A. 102 (2005) 15435–15440.
[57] B.S. Glick, C. Wachter, G.A. Reid, G. Schatz, Import of cytochrome b2 to the mitochondrial intermembrane space: the tightly folded heme-binding domain makes import dependent upon matrix ATP, Prot. Sci. 2 (1993) 1901–1917.
[58] N. Mesecke, K. Bihlmaier, B. Grumbt, S. Longen, N. Terziyska, K. Hell, J.M. Herrmann, The zinc-binding protein Hot13 promotes oxidation of the mitochondrial import receptor Mia40, EMBO Rep. 9 (2008) 1107–1113.